https://doi.org/10.1016/j.enconman.2021.114756

Negative thermal-flux phenomenon and regional solar absorbing coating improvement strategy for the next-generation solar power tower

Qiliang Wang [1,*], Junchao Huang [1], Zhicheng Shen [1], Yao Yao [1], Gang Pei [2], Hongxing Yang [1,**]

[1] *Renewable Energy Research Group (RERG), Department of Building Services Engineering, The Hong Kong Polytechnic University, Hong Kong, China*

[2] *Department of Thermal Science and Energy Engineering, University of Science and Technology of China, Hefei 230027, China*

*,** Corresponding author.

E-mail address: hong-xing.yang@polyu.edu.hk (H. Y.); qiliang.wang@polyu.edu.hk (Q. W.)

Abstract

Solar power tower (SPT) is regarded as the most promising technology for applications in concentrating solar power. However, a significant decrease in the solar-thermal conversion efficiency of the tower receiver in the SPT system occurs at high operating temperatures due to the massive radiation heat loss caused. In this work, a detailed heat transfer model of the tower receiver was established, and the negative thermal-flux phenomenon was discovered in the tower receiver based on the verified simulation results. In this context, a novel improvement strategy for regional solar absorbing coating on the tower receiver was proposed to enhance the thermal performance of the tower receiver in the next-generation SPT system. Two kinds of novel tower receivers by changing conventional solar absorbing coating into the silver-based coating (novel receiver I) and black chrome-based coating (novel receiver II) at negative thermal-flux regions were proposed, investigated, and compared with the prototype tower receiver without changes. The overall thermal performance of three kinds of tower receivers was numerically analyzed under different solar irradiances, solar hours throughout the day, and seasons. The results demonstrated that both the novel tower receivers achieved breakthrough enhancements on the thermal performance compared with the prototype receiver, showing great potential for practical application. The negative thermal-flux regions accounted for

almost a quarter of the entire receiver surface. The annual average radiation heat losses from negative thermal-flux regions in the novel receivers I and II were effectively reduced by 93.00 and 53.14 %. Accordingly, the annual average heat gains and receiver efficiencies were significantly enhanced by 6.54 and 6.03 %, respectively.

Keywords: *Concentrating Solar Power (CSP); Solar Power Tower (SPT); Heat Transfer; Molten Salt; Solar Absorbing Coating*.

Nomenclature

A	Area, m^2	υ	Kinematic viscosity, m^2/s
c	Specific heat capacity, J/(kg·K)	**Abbreviation**	
D	Diameter, m	amb	Ambient
f	Fluid/ friction factor	conv	Convection
g	Gravitational acceleration, m/s^2	CSP	Concentrating solar power
h	Convection heat transfer coefficient, $W/(K·m^2)$	DNI	Direct normal irradiance, W/m^2
H	Height, m	fc	Forced convection
L	Length, m	Gr	Grashof number
m	Mass flow rate, kg/s	HTF	Heat transfer fluid
q	Heat flux, W/m^2	in	Inlet
Q	Heat flux, W	iw	Inner wall
T	Temperature, °C	MF	Multiple factor
v	Velocity, m/s	nc	Natural convection
W	Width, m	NTR	Negative thermal-flux region
Greek Symbols		Nu	Nusselt number
α_s	Solar absorptance	out	Outlet
β	Temperature coefficient, K^{-1}	ow	Outer wall
ε	Emittance	Pr	Prandtl number
η	Efficiency	rad	Radiation
λ	Thermal conductivity, W/(m·K)	RMSD	Root-mean-square deviation

μ	Dynamic viscosity, m^2/s	Re	Reynold number
ρ_f	Density, kg/m^3	SAC	Solar absorbing coating
ρ_s	Reflectance	SPT	Solar Power tower

1. Introduction

Concentrating solar power (CSP) has been proven a promising technology due to the unique features of cost-effective thermal storage and friendliness to the electrical grid [1, 2]. CSP has a small capacity of just 6.2 GW as of 2019 [3], but its learning rate by above 20 % is extremely high [4], demonstrating its great application potential in the foreseeable future. To date, the representative concentrating solar colletors used in the CSP include the tower collector [5, 6], parabolic trough collector [7-9], dish collector [10], and fresnel collector [11]. Among them, the tower collector, which is used in solar power tower (SPT) system, is regarded as the most promising technical mode in terms of potential reduction of the levelized cost of energy [12], thereby attracting increasing interest from researchers and investors.

The solar tower receiver, mounted on a tower with an elevation of hundreds of meters, is the core solar-thermal conversion equipment in the SPT system, responsible for receiving and absorbing the highly concentrating solar fluxes reflected from the surrounding heliostats on the ground [13]. Hence, the solar-thermal conversion performance of the tower receiver exerts a significant role in the overall techno-economic performance of the SPT system. However, the tower receiver faces a severe problem of thermal performance degradation at higher operating temperatures due to the rapid increase in radiation heat loss caused by temperature. At present, the outlet temperature of the tower receiver in the commercial SPT system generally reaches 560 °C by employing solar salt ($NaNO_3$-KNO_3, 60-40 wt%) as the heat transfer fluid (HTF) [14, 15]. To further enhance the operating temperature of the tower receiver and thus improve the generating efficiency of the power block, some novel HTFs such as other molten salts or liquid metals with higher stability points were developed for the next-generation SPT system [16-18]. For instance, the HTF of $MgCl_2$-KCl with a stability point above 800 °C has been widely investigated and assessed in the next-generation SPT integrated with supercritical carbon dioxide (sCO_2) Brayton cycle [19, 20], in which the tower receiver's outlet temperature could reach 700-800 °C [21]. According to Planck's law, the radiation heat of an object

increases with its temperature raised to the fourth power [20, 22]. With such a high operating temperature for the next-generation SPT, the radiation heat loss from the surface of the tower receiver [20, 22] significantly increases compared with the current SPT. Worse, the increasing heat loss would exceed the solar energy absorption for the receiver surface's partial regions receiving low-density solar irradiance, leading to negative heat gains at such regions and thus severely degrading the thermal performance of the next-generation SPT.

Yağli [23] examined the heat loss and thermal efficiency of a solar power tower with the outlet temperature up to 1800 °C. The calculated efficiencies of the tower receiver at receiver surface temperatures of 400 and 1800 °C were 91.3 and 45.9 %, respectively. The results demonstrated that the most important factor affecting the receiver efficiency was the exponentially increasing radiation heat losses. Christian et al. [24] proposed and studied four kinds of receiver configurations. The new receiver geometries had internal view factors between the finned structures, thus reducing the radiation heat loss. Accordingly, the increase in thermal efficiency of the finned structures versus the standard cylindrical receiver design reached nearly 4%. Other related literature [6, 25] also investigated new tower receivers with different structures to enhance thermal performance. However, it must be noticed that many new geometrical structures of tower receivers are complex and even impractical in applying the SPT.

The solar absorbing coating (SAC), which is deposited on the outer surface of the tower receiver (external type), exerts a crucial role in the radiation heat loss and solar radiation absorption for the tower receiver. Traditionally, one tower receiver uses only one kind of SAC. The current SPT plants generally employed a conventional coating of black Pyromark paint with a high solar absorptance (α_s) of 0.94 but simultaneously a high thermal emittance (ε_t) of 0.88 [20]. The black Pyromark paint is suitable for the current SPT with relatively low operating temperature because of the limited radiation heat loss caused, but not for the next-generation SPT. This is because a much higher operating temperature for the next-generation SPT will sharply increase radiation heat loss, leading to negative heat gains at partial regions of the tower receiver. In this context, many researchers have focused on developing more advanced SAC with lower thermal emittance for the next-generation SPT [26, 27]. For instance, the Lawrence Berkeley National Laboratory (LBNL) developed a new SAC (α_s=0.9,

ε_t=0.4) composed of a transparent conductive oxide layer and black chrome, which possessed the high-temperature stability of up to 900 °C [28]. The developed SAC with low thermal emittance can lower the radiation heat loss, but its decreased solar absorptance will incur much absorption loss of solar energy because of highly concentrating solar radiation on the tower receiver. As a result, the new SAC may also cause negative heat gains at partial regions of the tower receiver where the solar radiation absorption is lower than the heat loss, thus decreasing the tower receiver efficiency [29]. Therefore, using only one kind of SAC on the tower receiver, whether conventional or advanced, would cause negative effects on the thermal performance of partial regions in the tower receiver.

There have been no reports about the detailed heat gain analysis of the tower receiver by region and the verification of the negative heat gain phenomenon occurring in the tower receiver. In this work, a detailed heat transfer model of the tower receiver was established. And then, the negative thermal-flux (heat gain) phenomenon was verified, the negative thermal-flux regions (NTRs) were determined in theory. In this framework, a regional SAC improvement strategy, i.e., applying different SACs to different regions of the tower receiver, was proposed to tackle the problem of massive radiation heat loss in the next-generation SPT and simultaneously restrict the solar absorption loss, so as to improve the negative thermal-flux phenomenon and achieve a breakthrough enhancement in receiver efficiency.

Specifically, the Dunhuang 10 MW SPT system [30], a demonstration project using molten salt medium and supercritical CO_2 Brayton cycle, was used as a case study. The binary Mg-based molten salt ($MgCl_2$-KCl, 38-62 wt%) was selected as the HTF of the tower receiver. The annual thermal performance of the tower receiver was investigated based on the established heat transfer model. Then the negative thermal-flux phenomenon was verified at the edge regions of the tower receiver, which were named negative thermal-flux regions (NTRs). Furthermore, two kinds of coatings with low thermal emittance, namely, silver-based coating and black chrome-based coating developed by LBNL, were selected as the secondary coatings to replace the original Pyromark paint in the NTRs. The thermal performances of three kinds of tower receivers, namely, prototype receiver with black Pyromark paint, novel receiver I with regional silver-based coating, and novel receiver II with regional black chrome-based coating, were studied under different direct normal irradiances (*DNIs*), different solar hours in a typical weather day, and different seasons.

2. Geometry and Material

2.1 Dunhuang 10 MW SPT plant

Dunhuang 10 MW SPT plant is located in Dunhuang (40.15°N, 94.68°E), northwest of China. The aerial view of the SPT plant is exhibited in Fig. 1(a) [31]. It can be observed that the external-type central receiver is mounted on the top of the tower with a height of 138 m. The surrounding heliostats concentrate the incoming solar rays to the surface of the tower receiver. The molten salt thermal storage tanks, heat exchangers and power block are placed on the ground near the tower. The number of heliostats is 1525, and their distribution in the solar field is shown in Fig. 1(b) [32]. Both length (L_h) and width (W_h) of each heliostat are about 10.95 m, and the actual mirror area of each heliostat is 115.70 m^2. It is worth mentioning that the Dunhuang 10 MW SPT plant is renovating from a conventional steam Rankin cycle into a supercritical CO_2 Brayton cycle, demonstrating a fitting case for this study about the next-generation SPT technology.

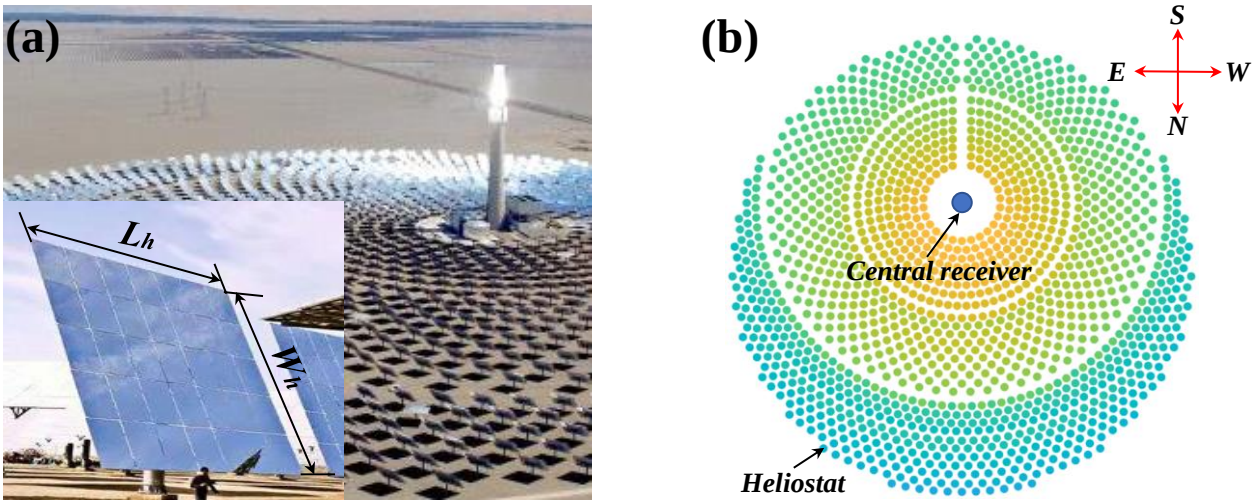

Fig. 1 Layout of Dunhuang 10 MW SPT plant: (a) Aerial view of the plant [31], (b) Heliostat distribution in the solar field [32].

2.2 Tower receiver

The tower receiver is the key component of the SPT system for realizing the solar-thermal conversion and thus providing the high-temperature heat for the subsequent power block. In the Dunhuang 10 MW SPT plant, the tower receiver has a height (H_{CR}) of 10.5 m and a diameter (D_{CR}) of 7.3 m. As shown in Fig. 2(a) and (b), the tower receiver is composed of 18 tube panels in the

circumferential. A single tube panel has a width (W_{panel}) around 1.29 m and consists of 31 tubes. It should be pointed out that only 5 tubes are displayed in a single tube panel in Fig. 2 to schematically represent 31 tubes. The outer and inner diameters of a single tube are 40 and 37.5 mm, respectively. Black Pyromark paint [33], generally regarded as a graybody with a diffuse surface, deposits on the outer surface of tubes for maximizing the absorption of concentrating solar irradiance. The back of the tube panels is set as the refractory wall.

According to the setup of the commercial SPT plant [34], 18 tube panels are divided into symmetrical two flow paths (flow path 1 and flow path 2), as shown in Fig. 2(b). Two inlets (inlet-1 and inlet-2) and outlets (outlet-1 and outlet-2) are located on the north and south sides of the tower receiver, respectively. The binary Mg-based molten salt ($MgCl_2$-KCl, 38-62 wt%) is selected as the HTF in this study. As mentioned above, the Mg-based molten salt has excellent thermal properties and competitive cost as the candidate for the advanced HTF in the next-generation SPT system [35, 36]. The Mg-based molten salt has a melting point of 424.4 °C and a high stability point above 800 °C. The HTF flows inside tubes and follows a serpentine flow pattern as exhibited in Fig. 3. In this study, the inlet and outlet temperatures (T_{in} and T_{out}) of the HTF are determined as 520 and 760 °C, respectively. The detailed geometrical and operating parameters of the tower receiver are included in Table 1.

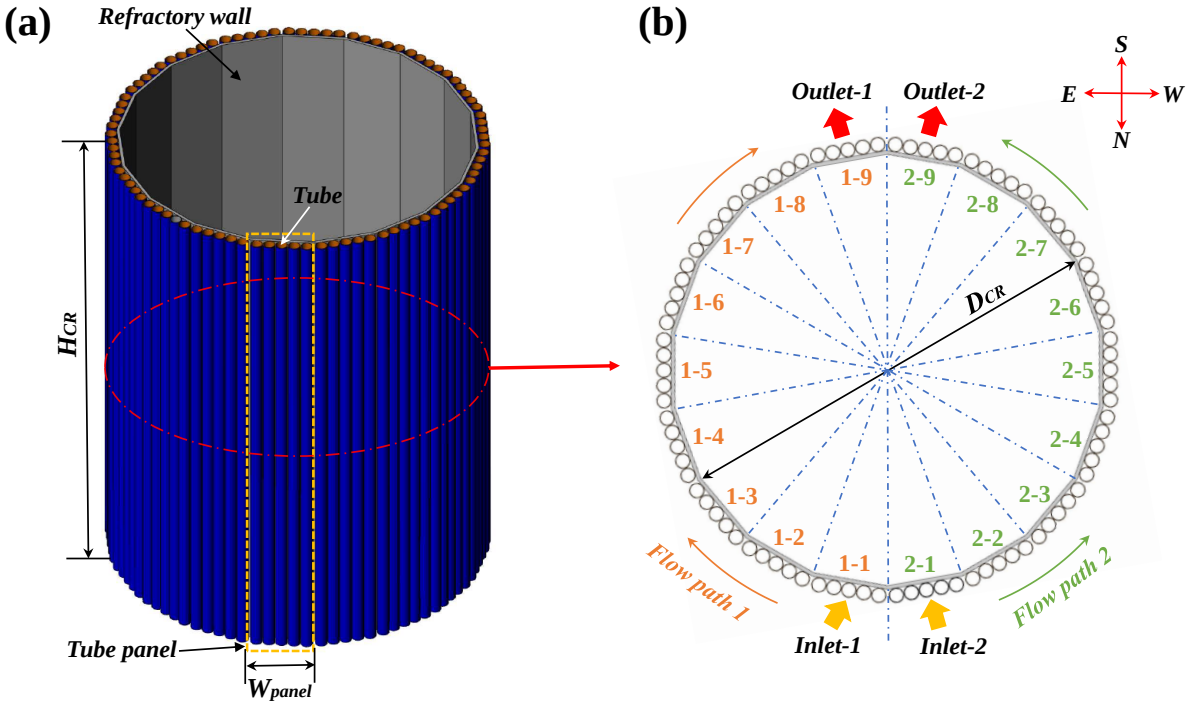

Fig. 2 Schematic diagram of the tower receiver: (a) Three-dimensional view, (b) Aerial view.

153 Table 1 Detailed geometrical and operating parameters of the tower receiver in Dunhuang 10 MW SPT tower [35]

Parameter	Value	Parameter	Value
Tower elevation	138 m	Outer diameter of single tube, $D_{tube,\ ow}$	40 mm
Number of heliostats	1525	Inner diameter of single tube, $D_{tube,\ iw}$	37.5 mm
Length (L_h) and width (W_h) of each heliostat	10.95 m	Pyromark paint's solar absorptance, α_s	0.94
Number of tube panels	18	Pyromark paint's thermal emittance, ε_t	0.88
Tube number per panel	31	HTF's melting point	424.4 °C
Receiver height, H_{CR}	10.50 m	HTF's stability point	> 800 °C
Receiver diameter, D_{CR}	7.30 m	Inlet temperature, T_{in}	520 °C
Width of single tube panel, W_{panel}	1.29 m	Outlet temperature, T_{out}	760 °C

154 # 3. Mathematical model and Method

155 In this study, an optical model of FluxSPT relying on the MCRT method was employed to
156 calculate the optical property of the solar field, i.e., detailed solar flux distribution projected on the
157 receiver surface [37]. The tool of FluxSPT was developed by Sánchez-González et al. to generate flux
158 maps caused by an entire field of heliostats, considering shading and blocking in addition to the rest
159 of optical losses. A 4-step methodology was presented to determine the flux density distribution on
160 central receivers of flat panels. This procedure relies on the oblique projection onto the receiver from
161 the flux distribution on the image plane, accomplished by a simple coordinate system transformation
162 [38]. The simulated results obtained based on the FluxSPT have been proven high accuracy compared
163 with Plataforma Solar de Almería measurements and SolTrace simulations [39].

164 In this section, a detailed heat transfer model of the tower receiver will be established, and Its
165 prediction performance will be verified by comparing the simulated results with the experimental data
166 of the Solar Two plant [40].

167 ## 3.1 Heat transfer model and method

In the SPT, the heat transfer characteristics have vast differences in different regions of the tower receiver due to highly non-uniform solar flux and temperature distributions on the receiver surface [41]. To fully observe the receiver's heat transfer characteristics at different positions, the cylindrical tower receiver surface is spread out from the southernmost line and thus forming a two-dimension receiver surface, then the receiver surface is divided into 13 horizontal rows and 36 vertical columns, a total of 468 equal regions as exhibited in Fig. 3. Each rectangular region has a moderate length (Δx) and height (Δy) of 0.645 and 0.810 m, respectively. The number of 468 rectangular regions was selected for practical engineering, calculation accuracy, and computing speed. On the first hand, the region with such moderate dimensions contributes to the practical operating of the improvement strategy in engineering, mass production, and processing. On the other hand, a moderate number of regions can effectively save computation time on the premise of calculation accuracy.

It is worth mentioning that one vertical column covers half of the single tube panel, i.e., 15.5 tubes, which is denoted as a multiple factor (MF) of tubes in a single region. In the center of each region, there is a computation node with a coordinate number expressed with row and column numbers, such as the first node on the top left (*1, 1*) and the last one on the bottom right (*12, 36*). In this context, a detailed heat transfer model of the tower receiver is established by C++ codes.

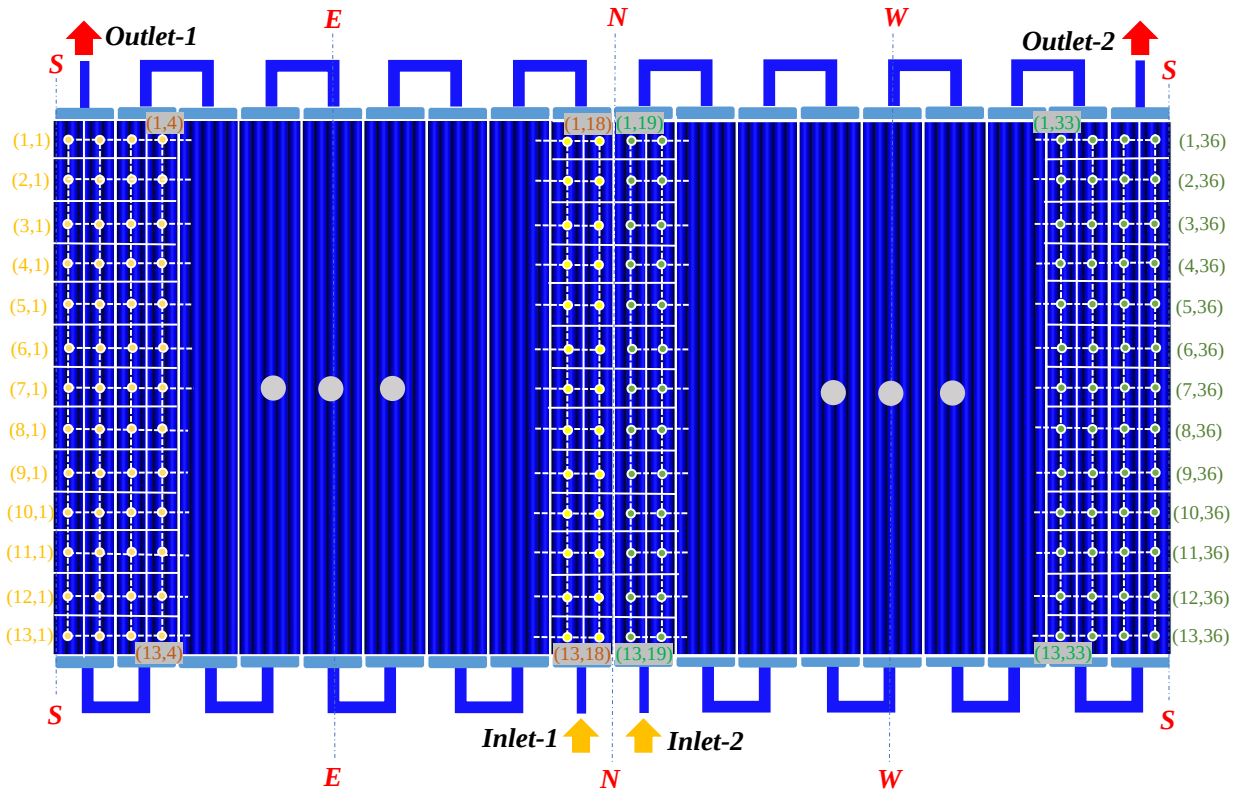

Fig. 3 Division and space discretization of receiver surface

Based on the obtained receiver surface's solar flux distribution from the FluxSPT model, the solar irradiance received by the one rectangular region at the position of (i, j) can be calculated as follows:

$$Q_{received}(i, j) = q_{solar}(i, j)\Delta x \triangle y \quad (i=1\sim13, j=1\sim36), \tag{1}$$

where (i, j) refers to the coordinate number, $Q_{received}(i, j)$ and $q_{solar}(i, j)$ represent the solar irradiance received, W, and the solar flux received, W/m^2, in the specific region (i, j).

The solar flux projected on the receiver surface will then be partially absorbed by the tubes, the other part will be reflected by the tubes and eventually dissipated to the environment:

$$Q_{received}(i, j) = Q_{absorbed}(i, j) + Q_{reflected}(i, j)\ , \tag{2}$$

$$\begin{cases} Q_{absorbed}(i, j) = \alpha_s Q_{received}(i, j) \\ Q_{reflected}(i, j) = \rho_s Q_{received}(i, j) \end{cases}, \tag{3}$$

where $Q_{absorbed}$ and $Q_{reflected}$ are the solar irradiances absorbed and reflected, respectively, W; α_s and ρ_s refer to the solar absorptance and reflectance of the SAC covered on the outer surface of tubes. One part of the thermal energy of the receiver by absorbing the solar irradiance will be transferred to the

HTF inside the tubes by the conductive and convective heat transfer modes, eventually becoming the heat gain of the HTF (Q_{HTF}). It is worth noting that the value of Q_{HTF} could become negative if the heat loss (Q_{loss}) is higher than the solar irradiance absorbed ($Q_{absorbed}$). The other part of the thermal energy will lose to the ambient mainly by the radiative and convective heat transfer modes (Q_{loss}). The heat transfer processes can be expressed as follows:

$$Q_{absorbed}(i,j) = Q_{HTF}(i,j) + Q_{loss}(i,j)\,, \tag{4}$$

$$Q_{HTF}(i,j) = Q_{cond,ow-iw}(i,j) = Q_{conv,iw-HTF}(i,j)\,, \tag{5}$$

$$Q_{loss}(i,j) = Q_{rad,ow-amb}(i,j) + Q_{conv,ow-amb}(i,j)\,. \tag{6}$$

In Eqs. (5) and (6), $Q_{cond,ow\text{-}iw}$ is the conductive heat transfer from the outer wall (*ow*) to the inner wall (*iw*) of the tubes, and $Q_{conv,iw\text{-}HTF}$ represents the convective heat transfer between the inner wall of the tubes and the HTF, W. $Q_{rad,ow\text{-}amb}$ and $Q_{conv,ow\text{-}amb}$ refer to the radiation and convective heat losses from the outer wall to the ambient, W. The computations of these four heat transfer powers will be introduced in detail as follows.

The value of $Q_{cond,ow\text{-}iw}$ at the whole region (*i, j*) can be calculated by the product of conductive heat transfer per tube and the multiple factor (MF, equal to 15.5 in this study):

$$Q_{cond,ow-iw}(i,j) = \frac{2\pi\Delta y\lambda_{tube}(T_{ow}-T_{iw})}{\ln(D_{tube,iw}/D_{tube,ow})} \times MF\,, \tag{7}$$

where T_{ow} and T_{iw} represent the temperatures of the outer wall and inner wall of the tubes, K; λ_{tube} is the thermal conductivity of the tube material, W/(m·K).

Similarly, $Q_{conv,iw\text{-}HTF}$ can be expressed by Eq. (8),

$$Q_{conv,iw-HTF}(i,j) = \pi D_{tube,iw}\Delta y h_f (T_{iw}-T_f) \times MF\,, \tag{8}$$

where T_f represents the HTF temperature, K; and h_f is the convective heat transfer coefficient of HTF, W/(m^2·K), which can be calculated by following formulas [42]:

220 $$\begin{cases} h_f = \dfrac{Nu_f \lambda_f}{D_{tube,iw}} \\ Nu_f = \dfrac{(f/8)(Re_f - 1000)Pr_f}{1+12.7(f/8)^{1/2}(Pr_f^{2/3}-1)} \\ f = 1 \Big/ (0.79 \ln Re_f - 1.64)^2 \\ Re_f = \dfrac{\rho_f v_f D_{tube,iw}}{\mu_f} \end{cases}, \quad (9)$$

221 where λ_f is the thermal conductivity of the HTF, W/(m·K), ρ_f is the density of the HTF, kg/m^3, μ_f is the
222 dynamic viscosity of the HTF, m^2/s, v_f represents the flow velocity of the HTF in a single tube, m/s;
223 Nu_f, Re_f, and Pr_f are the Nusslt number, Reynolds number, and Prandtl number of HTF, f represents the
224 friction factor of the inner wall in the tubes.

225 The value of $Q_{rad,ow\text{-}amb}$ can be computed by Eq. (10),

226 $$Q_{rad,ow-amb}(i,j) = \frac{\sigma(T_{ow}^4 - T_{amb}^4)}{\dfrac{1-\varepsilon_t}{\varepsilon_t A_{ow}} + \dfrac{1}{A_{ow}}} \times MF, \quad (10)$$

227 where T_{amb} represents the ambient temperature, K; ε_t is the thermal emittance of the solar absorbing
228 coating; and A_{ow} refers to the area of the outer wall of the single tube, m^2.

229 The value of $Q_{conv,ow\text{-}amb}$ can be obtained by the following Eq.(11):

230 $$Q_{conv,ow-amb}(i,j) = h_c A_{ow}(T_{ow} - T_{amb}) \times MF, \quad (11)$$

231 where h_c represents the combined convective heat transfer coefficient of the receiver surface,
232 W/(m^2·K), considering the forced and natural convective heat transfers of air on the receiver surface.
233 The value of h_c can be calculated by the expressions as follows [32, 43]:

234 $$h_c = (h_{fc}^{3.2} + h_{nc}^{3.2})^{1/3.2}, \quad (12)$$

235 $$\begin{cases} h_{fc} = \dfrac{\lambda_{amb-ow} Nu_{fc}}{D_{CR}} \\ Nu_{fc} = 0.0455 Re_{fc}^{0.81} \\ Re_{fc} = \dfrac{v_{wind} D_{CR}}{\mu_{amb}} \end{cases}, \quad (13)$$

$$\begin{cases} h_{nc} = \dfrac{\lambda_{amb} Nu_{nc}}{H_{CR}} \\ Nu_{nc} = 0.049\pi Gr_{nc}^{1/3} (T_{amb} / T_{ow})^{0.14} \\ Gr_{nc} = \dfrac{g\beta(T_{ow} - T_{amb}) H_{CR}^3}{\upsilon_{amb}^2} \end{cases}, \quad (14)$$

where h_{fc} and h_{nc} represent the forced and natural convective heat transfer coefficients, W/(m^2·K). $\lambda_{amb\text{-}ow}$ refers to the thermal conductivity of air with a combined consideration of ambient temperature and receiver temperature, μ_{amb} is the dynamic viscosity of air, m^2/s, v_{wind} represents the incoming wind velocity, m/s. λ_{amb} is the thermal conductivity of air with a consideration of only ambient temperature, W/(m·K). Gr is the Grashof number, g and υ_{amb} are the gravitational acceleration and kinematic viscosity of air, respectively, m/s^2, m^2/s. β is the temperature coefficient, K^{-1}, the value of β equals $1/T_{amb}$.

According to Eqs. (4)-(6) integrated with Eqs. (1), (3), and (7)-(14), all temperatures and heat transfer powers involved in the models can be figured out. Subsequently, the heat balance equation of the HTF, i.e., the heat gain of the HTF ($Q_{gain,HTF}$), in a specific region (i, j) can be expressed:

$$\begin{cases} Q_{conv,iw-HTF}(i,j) = Q_{HTF}(i,j) \\ Q_{HTF}(i,j) = c_{p,f} m_f (T_{out}(i,j) - T_{in}(i,j)) \times MF \end{cases}, \quad (15)$$

where $c_{p,f}$ is the specific heat of the HTF, J/(kg·K); m_f is the mass flow rate of HTF in a single tube, kg/s. It should be noted that the values of m_f in flow paths 1 and 2, depending on the actual solar flux and environmental conditions, are different. T_{out} and T_{in} represent the outlet and inlet temperatures of the region (i, j). In the iterative calculations of the model, the T_{in} (i, j) is the outlet temperature of the previous region.

In the above equations, the related thermal properties of the HTF of binary molten salt of $MgCl_2$-KCl will vary with the different HTF temperatures, which can be calculated by the following equations [44]:

$$\rho_f = 1903.7 - 0.552T_f, 450°\text{C} \le T_f \le 800°\text{C}, \quad (16)$$

$$c_{p,f} = 989.6 + 0.1046T_f, 450°\text{C} \le T_f \le 800°\text{C}, \quad (17)$$

$$\lambda_f = 0.5047 - 0.0001T_f, 450℃ \le T_f \le 800℃, \quad (18)$$

$$\mu_f = 0.014965 - 2.91\times10^{-5}T_f + 1.78\times10^{-8}T_f^2, 450℃ \le T_f \le 800℃. \quad (19)$$

Based on the above model, the mass flow rates in flow paths 1 and 2, all temperatures and heat transfer powers for different regions and whole receiver can be obtained by iterative calculations. In actual calculation processes, the simulated results are regarded as available once both outlet-1 and outlet-2 temperatures of the two flow paths are in the range of 760-760.5 °C. Otherwise, the mass flow rates will be changed, then iterative calculations will be repeated. As a result, the total solar irradiance received, total radiation heat loss, total convective heat loss and total heat gain by the HTF can be calculated by the expressions:

$$Q_{received} = \sum_{i=1}^{i=13}\sum_{j=1}^{j=36} Q_{received}(i,j), \quad (20)$$

$$Q_{rad,ow-amb} = \sum_{i=1}^{i=13}\sum_{j=1}^{j=36} Q_{rad,ow-amb}(i,j), \quad (21)$$

$$Q_{conv,ow-amb} = \sum_{i=1}^{i=13}\sum_{j=1}^{j=36} Q_{conv,ow-amb}(i,j), \quad (22)$$

$$Q_{HTF} = \sum_{i=1}^{i=13}\sum_{j=1}^{j=36} Q_{HTF}(i,j). \quad (23)$$

And the receiver efficiency (η) is defined by:

$$\eta = \frac{Q_{HTF}}{Q_{received}}. \quad (24)$$

3.2 Model validation

In this section, the Solar Two plant, a famous SPT plant located in Mojave Desert [40], was selected as the study case to validate the above heat transfer model by comparing the experimental data with the simulated results. The tower receiver in the Solar Two plant has a height of 6.20 m and a diameter of 5.14 m. It is composed of 24 tube panels, and one single tube panel consists of 32 tubes. The outer surface of the receiver is deposited with the conventional black Pyromark paint, and the tower receiver employs the solar salt ($NaNO_3$-KNO_3, 60-40 wt%) as the HTF. The detailed geometrical parameters and thermal properties of the HTF can be found in the literature [20, 44]. In this section, all parameters in the models used the corresponding parameters in the actual Solar Two plant. Four

test cases reported in [40] were selected to carry out the comparisons. The detailed environmental and operating parameters in the four test cases are presented in Table 2. In this study, the relative error and root-mean-square deviation (*RMSD*) were employed to evaluate the accuracy of the simulation results [45, 46]:

$$RMSD = \sqrt{\frac{\sum_{i=1}^{i=n}[(x_{sim,i} - x_{exp,i})/x_{\exp,i}]^2}{n}}, \tag{25}$$

where x_{sim} and x_{exp} represent the simulated and experimental data, respectively; n is the total data number, it equals 4 in this study.

As shown in Table 2, the relative errors of the simulated results compared with the experimental results remain within ± 2 %, and the value of *RMSD* is only 1.67, demonstrating that the simulated results yield consistencies with the experimental data, and the heat transfer model possesses good prediction ability for the thermal performance of SPT system.

Table 2 Comparisons between the experimental and simulated results [40]

Case	Test date	T_{in} (°C)	T_{out} (°C)	*DNI* (W/m^2)	T_{amb} (°C)	v_{wind} (m/s)	m (kg/s)	η-measured	η-calculated	Relative error (%)	*RSMD* (%)
1	29-Sep-97	295	551	913	32	0.6	80	0.888	0.895	0.79	0.72
2	30-Sep-97	301	550	975	33	1.0	90	0.884	0.878	−0.68	
3	05-Mar-99	308	564	989	16	3.0	81	0.866	0.873	0.81	
4	12-Mar-99	303	563	898	14	1.8	67	0.881	0.876	−0.57	

4. Results and discussions

4.1 Negative thermal-flux phenomenon and negative thermal-flux region

Relying on the FluxSPT and heat transfer model, the solar flux distribution and thermal performance of the tower receiver in 60 days, selected throughout the year [47], were calculated. Then the annual average solar flux distribution and heat transfer metrics of the tower receiver can be

predicted through heavy computations. The obtained annual average results contribute to obtaining the universal rules of heat transfer characteristics for the next-generation SPT.

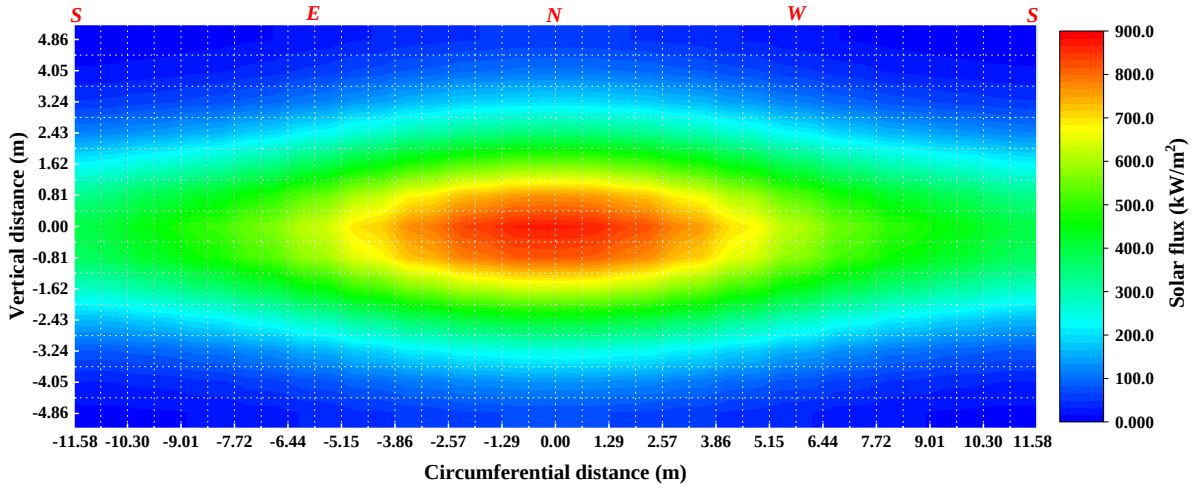

Fig. 4 Annual average solar flux distribution on the receiver surface

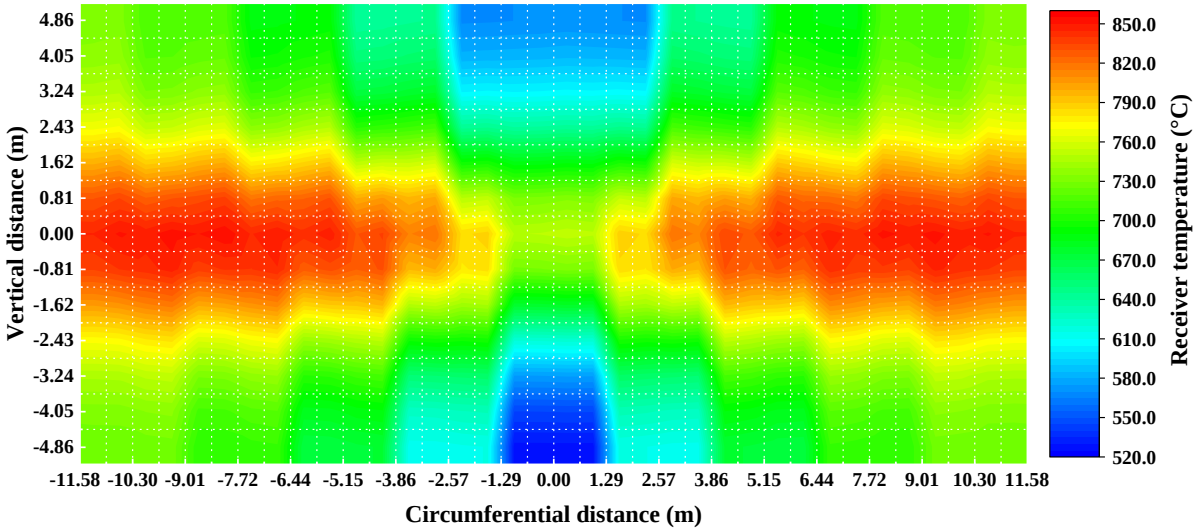

Fig. 5 Annual average receiver temperature (T_{ow}) distribution on the receiver surface

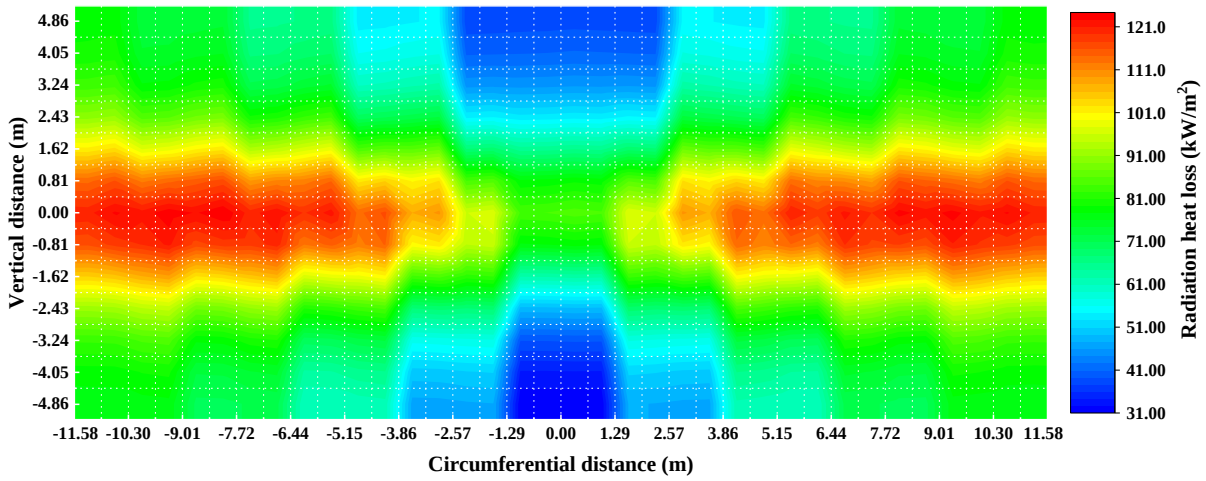

Fig. 6 Annual average radiation heat loss distribution on the receiver surface

According to Energyplus weather information [47], the annual *DNI* in Dunhuang is 1777 kWh/m^2 with annual 3257 sunshine hours. As exhibited in Fig. 4, the annual average solar flux distribution shows the highly non-uniform feature on the receiver surface. The concentrating ratio reaches almost 1500 at the regions located in the center of the northern side while only around 7-10 at the edge regions. Furthermore, the distribution of receiver temperature, i.e., the temperature of the outer wall of tubes, is also obtained as shown in Fig. 5. It can be observed that the non-uniform feature of the receiver temperature is completely different from that of the solar flux, showing high temperatures at the southern side but relatively low temperatures at the northern side. The lowest receiver temperature occurs at two inlets of flow paths 1 and 2, corresponding to the receiver's circumferential regions from −1.29 to 1.29 m and vertical distance of −4.86 m. The highest receiver temperature appears in the middle regions of the southern side. The lowest and highest receiver temperatures are 528 and 854 °C, with a temperature difference of nearly 330 °C. According to Eq. (10), the radiation heat loss from the receiver is in direct proportion to the receiver temperature raised to the fourth power. It is thereby predictable that the radiation heat loss from the receiver in this next-generation SPT will be much higher than the conventional receiver in the current-generation SPT due to much higher HTF and receiver temperatures. As exhibited in Fig. 6, the radiation heat loss distribution is similar to the receiver temperature distribution. It is calculated that the average radiation heat loss is about 80.5 kW/m^2, 17.3 times the convective heat loss.

Due to the mismatched distributions of solar flux and radiation heat loss, the map of the annual average net heat gain of the HTF (i.e., the net thermal flux of the receiver), as shown in Fig. 7, appears an interesting phenomenon, that is, the negative thermal-flux phenomenon at the edge regions of the receiver. That is because these edge regions only receive extremely low solar flux but emit high radiation heat loss; consequently, the net heat gain of the HTF appears negative at these edge regions when the total heat loss exceeds the absorbed solar flux. This phenomenon and these edge regions are conceptually named negative thermal-flux phenomenon and negative thermal-flux regions (NTRs), respectively. The NTRs are exhibited in Fig. 7 with hatched regions. Herein, different slash densenesses are used to indicate the intensity of the negative thermal-flux phenomenon. High-, middle-, and low-density slashes represent the net heat gain in the ranges of −80~−53, −53~−26, and −26~0 kW/m^2, demonstrating the severely, moderately, and mildly negative thermal-flux phenomena, respectively. It can be observed that the number of the NTR reaches 111, almost a quarter of the entire receiver, of which the numbers of severe, moderate, and mild NTRs are 42, 34, and 35, respectively, demonstrating that the negative thermal-flux phenomenon is quite severe. By calculations, the total absorbed solar flux, total radiation heat loss, and total heat gain in the NTRs are about 2.01, 4.14, and −2.47 MW, respectively, indicating that radiation heat loss is the major factor resulting in the negative thermal-flux phenomenon.

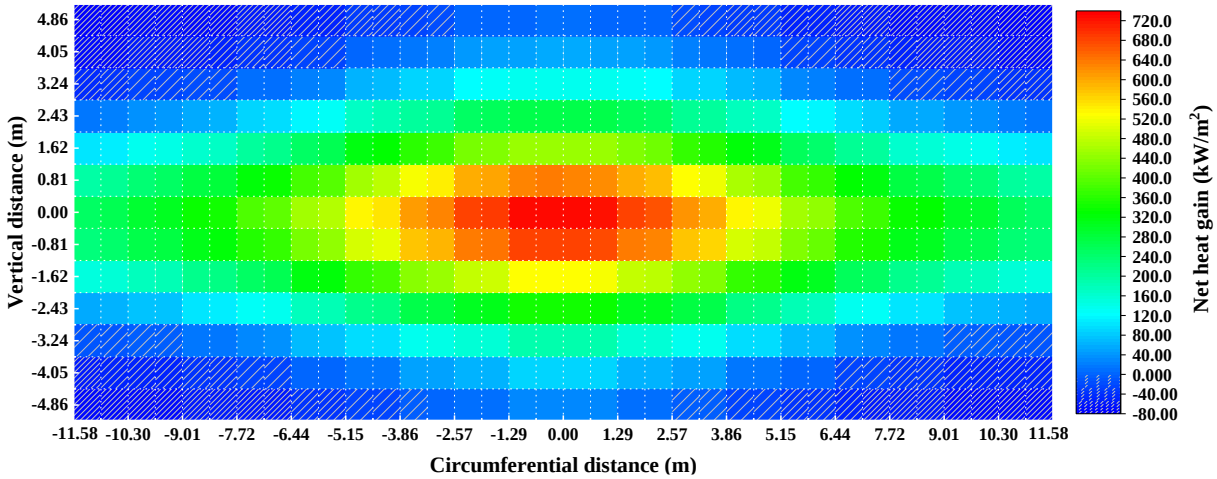

Fig. 7 Net heat gain map and negative thermal-flux regions (hatched regions) on the receiver surface

4.2 Solar absorbing coating improvement in the NTRs

The severe negative thermal-flux phenomenon occurring in the tower receiver reveals that the conventional SAC of black Pyromark paint is no more suitable for the NTRs in the tower receiver. Aiming to effectively improve the negative thermal-flux phenomenon in the NTRs and thus enhance the receiver efficiency, a novel improvement strategy for the tower receiver, that is, changing the black Pyromark paint in the NTRs into secondary coating with lower thermal emittance but no changing in other regions, was proposed. Two kinds of secondary coatings, i.e., silver (Ag) film and black chrome coating, are selected in this study to validate the above hypothesis. Ag-based coating, composed of Ag layer and SiO_2 protective film, is a popular material [48]. As explained in the introduction, the black chrome-based coating, composed of a transparent conductive oxide layer and black chrome, was developed by Lawrence Berkeley National Laboratory (LBNL) in 2018 [23]. As presented in Table 3, Ag-based and black chrome-based coatings have an ultra-low and medium-low thermal emittance of 0.06 and 0.40@700°C. Simultaneously, the solar absorptivities of both coatings are compromised to 0.20 and 0.90 as well. The aims of selecting these two types of coatings are to verify the improvement effects of the extreme and advanced selectivity characteristics of coatings on the negative thermal-flux regions in the tower receiver, respectively.

Table 3 Thermal properties of three kinds of solar absorbing coatings

Parameter	Black Pyromark paint	Ag-based coating	Black chrome-based coating
α_s	0.94	0.20	0.90
ε_t	0.88	0.06	0.40

In this framework, relying on the established model, the heat transfer characteristics of the novel receiver I with Ag-based coating changes in the NTRs and novel receiver II with black chrome-based coating changes in the NTRs are calculated and compared with the prototype receiver without changes. The net heat gain maps of the novel receivers I and II are exhibited in Fig. 8 and Fig. 9, respectively. It can be observed that the negative thermal-flux phenomena of novel receivers I and II are effectively improved and even eliminated compared with those of the prototype receiver in Fig. 7. The numbers of the NTRs are 84 and 64 in the novel receivers I and II, which is effectively reduced compared with the prototype receiver. Besides, all NTRs in the novel receiver I are improved to a mild level. The

severe and moderate NTRs in the novel receiver II are improved to moderate and mild levels, respectively.

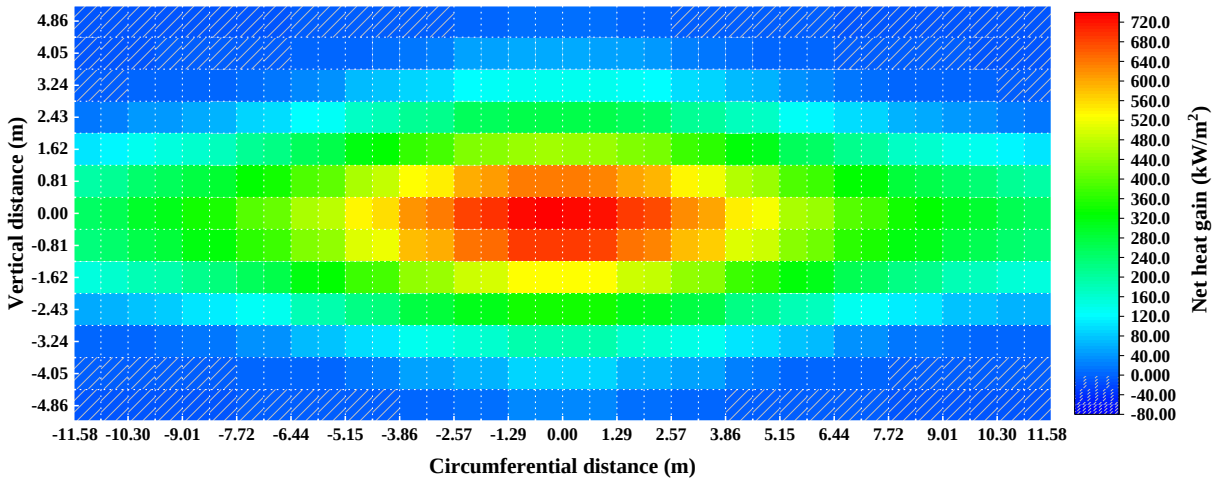

Fig. 8 Net heat gain map of novel receiver I with Ag-based coating changes in the NTRs

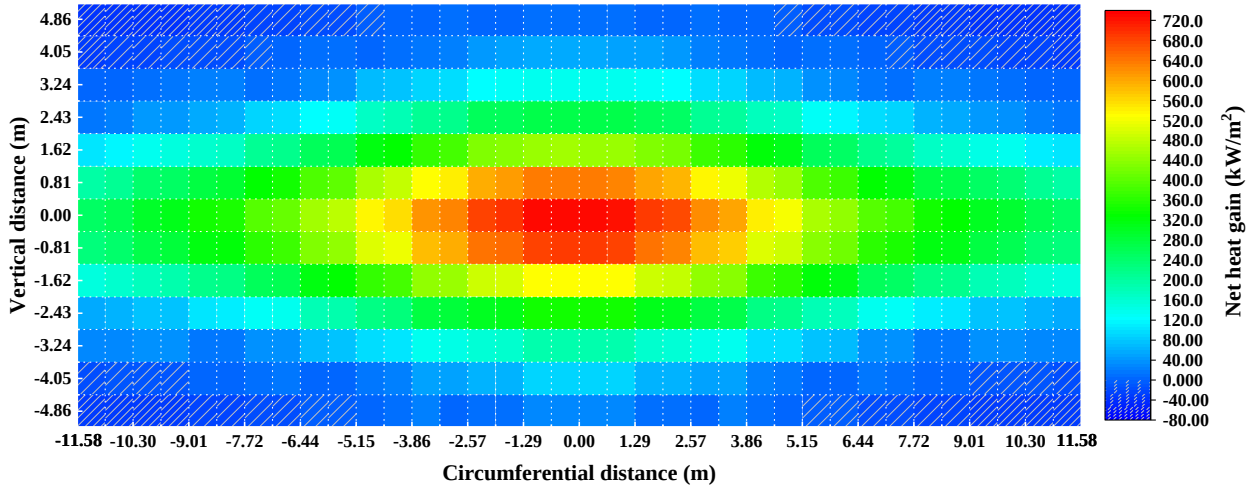

Fig. 9 Net heat gain map of novel receiver II with black chrome-based coating changes in the NTRs

In addition, the operating parameters and heat transfer metrics of the prototype and novel receivers are calculated and presented in Table 4. It can be observed that the outlet-1 and outlet-2 temperatures are well controlled within an acceptable range of 760.0~760.5 °C by adjusting the mass flow rates of flow paths 1 and 2. Through the secondary coating improvements, the radiation heat losses of the regions covered with the secondary coating are effectively reduced from 4.14 MW in the prototype receiver to 0.29 and 1.94 MW by about 93.00 and 53.14 % in novel receivers I and II, respectively. Due to the reduced solar absorptance of secondary coatings, the amount of solar irradiance absorbed by regions with secondary coating in the novel receiver I and II decrease by 78.61 and 4.48 %.

However, the solar absorption losses caused by the secondary coatings are limited because of the relatively low-density solar flux projecting on these edge regions. As a result, great successes of improving the negative heat gains in the novel receivers I and II are achieved. The net heat gains of regions with secondary coating in novel receivers I and II are enhanced to −0.20 and −0.37 MW from −2.47 MW of that in prototype receiver. From the perspective of the whole tower receiver, the total absorbed solar irradiances by the novel receivers I and II only have relative decreases by 2.84 and 0.14 % compared with that by the prototype receiver. That is because the regions with the secondary coating receive low-density solar fluxes, the secondary coatings with reduced solar absorptances will thereby not cause too much absorption loss of solar irradiance. In contrast, the total radiation heat losses from the novel receivers I and II are effectively reduced by 22.38 and 13.64 %, respectively. Because of the excellent performance exerted by the regional SAC improvement method, the annual average of heat gains and receiver efficiencies of novel receivers I and II have breakthrough enhancements by 6.54 and 6.03 %, which is higher than 3-4% of enhancement in receiver efficiency in the previous literature [20, 24].

Table 4 Operating parameters and heat transfer metrics of prototype and novel receivers

Item	Prototype Receiver	Novel Receiver I	Novel Receiver II	Improvement percentage of Receiver I (%)	Improvement percentage of Receiver II (%)
Inlet-1/2 temperature (°C)		520.0		\	
Outlet-1 temperature (°C)	760.46	760.29	760.48	\	
Outlet-2 temperature (°C)	760.34	760.27	760.32	\	
m in flow path 1 (kg/s)	82.77	88.35	87.73	6.74	5.99
m in flow path 2 (kg/s)	81.53	86.80	86.49	6.46	6.08
Number of NTR	111	84	64	\	
Radiation heat loss in regions with secondary coating (MW)	4.14	0.29	1.94	−93.00	−53.14
Solar flux absorbed in regions with secondary coating (MW)	2.01	0.43	1.92	−78.61	−4.48
Heat gain in regions with secondary coating (MW)	−2.47	−0.20	−0.37	\	
Total solar irradiance received (MW)		67.94		\	

Total solar irradiance absorbed (MW)	63.83	62.25	63.74	−2.48	−0.14
Total radiation heat loss (MW)	19.57	15.19	16.90	−22.38	−13.64
Total convection heat loss (MW)	1.13	1.12	1.12	\	
Total heat gain (MW)	42.81	45.61	45.39	6.54	6.03
Receiver efficiency (%)	**63.02**	**67.14**	**66.82**	**6.54**	**6.03**

4.3 Thermal performance at different *DNIs*

Because the secondary coatings of Ag-based and black chrome-based coatings have reduced solar absorptivities, the *DNI* may affect the overall thermal performance of the novel receivers. In this section, the influences of different *DNIs* on the thermal performance of the novel receivers are investigated. The noon of the summer solstice is selected in this analysis. Besides, the ambient temperature, wind velocity, inlet and outlet temperatures are determined as the same values as those set in sections 4.1 and 4.2, i.e., 15 °C,1.0 m/s, 520 and 760 °C, respectively. The calculated results are exhibited in Fig. 10.

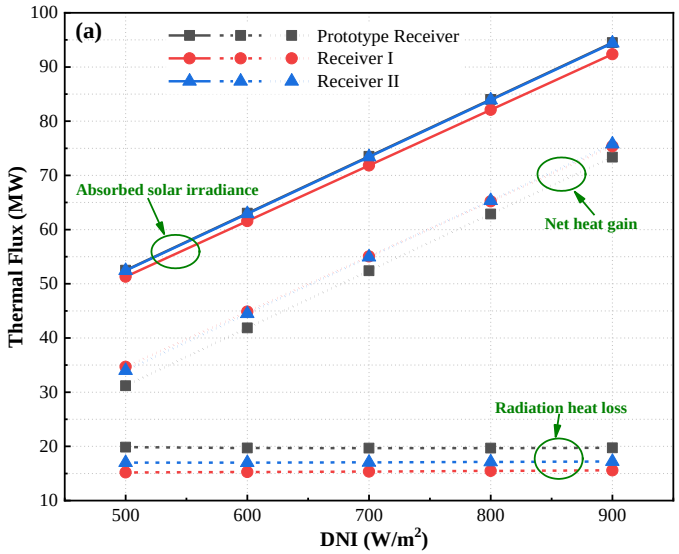

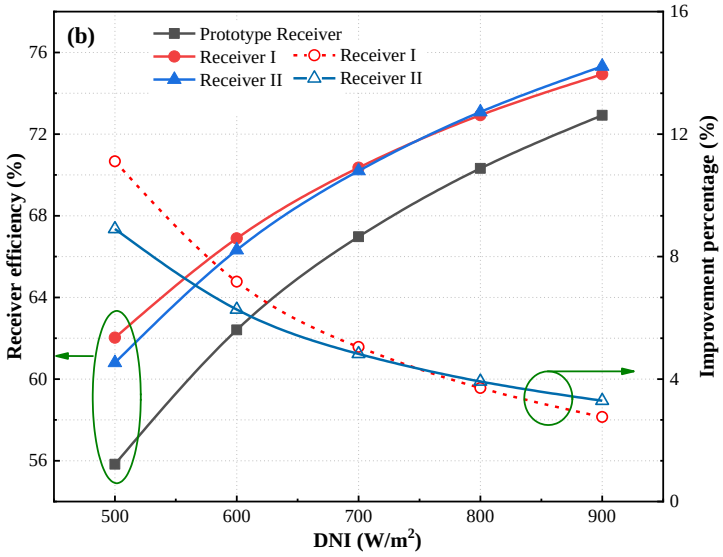

Fig. 10 Thermal fluxes and receiver efficiencies of three kinds of receivers at different *DNIs* on the noon of the summer solstice

As shown in Fig. 10(a), with the increasing *DNIs* from 500 to 900 W/m^2, the absorbed solar irradiances by the novel receiver II have no distinguished differences from those by the prototype receiver, but the absorbed solar irradiances by the novel receiver I are obviously lower than those by the prototype receiver and the differences between the two gradually increase. That is because a much lower solar absorptance of only 0.2 in the Ag-based coating causes much more solar absorption loss with the increase of *DNIs*. In contrast, the radiation heat losses of three kinds of receivers almost have no variations with different *DNIs*. Accordingly, the novel receiver I achieves the largest heat gains at the lower *DNIs*. With the increase of *DNIs*, novel receiver II surpasses receiver I and gets the largest heat gain. As shown in Fig. 10(b), with the increasing *DNIs*, both novel receivers I and II obtain superior thermal performance but with a diminishing advantage compared with the prototype receiver. The novel receiver I possesses the best performance at low *DNIs* below 750 W/m^2 owing to the ultra-low thermal emittance of Ag-based coating and limited solar absorption loss. The receiver efficiencies of novel receivers I, II and prototype receiver are 62.03, 60.80 and 55.83 % at *DNI* of 500 W/m^2, respectively. Accordingly, improvement percentages in the efficiency of the former two novel receivers reach 11.11 and 8.9 %, respectively. With the *DNI* exceeding 750 W/m^2, the novel receiver II surpasses the novel receiver I as the best-performing one. This mainly attributes to much less solar absorption loss incurred by the black chrome-based coating than Ag-based coating at high *DNIs*. The receiver

efficiencies of novel receivers I, II, and prototype receiver are 74.93, 75.32, and 72.92 % at *DNI* of 900 W/m^2, respectively. Accordingly, the efficiency improvement percentages of the former two novel receivers reach 2.76 and 3.29 %.

4.4 Thermal performance at different solar hours

In a typical day, the solar flux distribution on the tower receiver varies with solar hours, thereby affecting the thermal performance of the novel receivers I and II. In this section, the typical day of the summer solstice is selected to investigate the influence of different solar hours on the novel receivers I and II. The detailed *DNIs* at solar hours from 8 to 16 h on the summer solstice are presented in Table 5, and the calculated receiver efficiency results are exhibited in Fig. 11.

Table 5 *DNIs* at different solar hours on the summer solstice

Solar hour/h	8	9	10	11	12	13	14	15	16
DNI/W·m^{-2}	584	645	744	799	825	802	794	769	662

As shown in Fig. 11, both novel receivers I and II maintain superior thermal performance throughout the day. Particularly in the morning and evening, two novel receivers obtain more excellent performance. The first reason for this phenomenon is the low *DNI* at solar hours of 8-9 and 15-16 h; as explained above, lower *DNI* is conductive to exert superior performance for the novel receivers, particularly for the novel receiver I. In addition, the center of solar flux distribution will shift to the receiver's western side and eastern side in the morning and evening hours, which will inevitably affect the work of the secondary coating. As the solar hour comes to 10 h, the novel receiver II catches up with the novel receiver I, and exerts the best thermal performance afterward. That is mainly because the higher *DNIs* make it easier for the novel receiver II to play the effectiveness. Both novel receivers achieve the maximum and minimal efficiency improvements at solar hours of 8 h and 12 h, respectively. Specifically, the improvement percentages in the efficiency for the novel receivers I and II are 8.67 and 8.03 %, 3.42 and 3.74 % at 8 and 12 h, respectively.

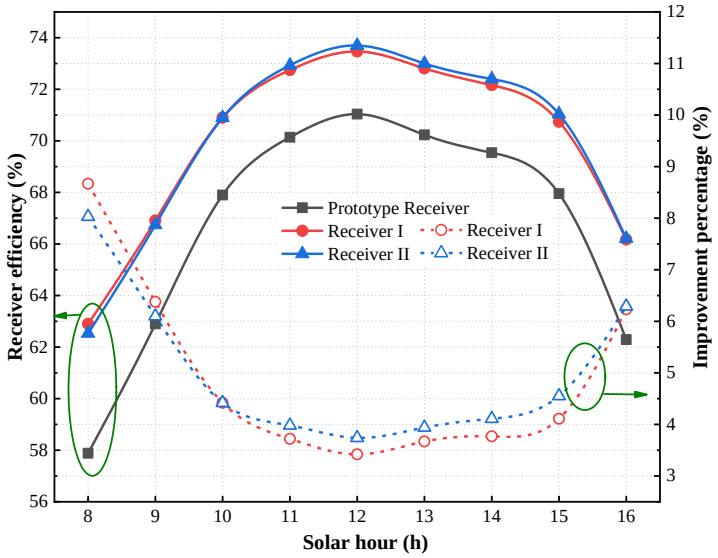

Fig. 11 Receiver efficiencies of three kinds of receivers at different solar hours on the summer solstice

4.5 Thermal performance at different seasons

Besides different solar hours throughout the day, the solar flux distribution is also affected by the different seasons throughout the year. In this section, spring equinox, summer solstice, and winter solstice are selected as the representative days in different seasons. And the noons of three days are selected as the representative solar hour to investigate the thermal performance of the novel receiver. It should be noted that the solar flux distributions on the autumn equinox are the same as the spring equinox; thus, the autumn equinox is not presented in this section. In this section, the *DNIs* at the noons of three representative days are set as 700 W/m^2. The other environmental and operating parameters are the same as the settings in the above sections.

The calculated receiver efficiency results are exhibited in Fig. 12. Three kinds of receivers achieve the highest receiver efficiencies at the summer solstice but the lowest efficiencies at the winter solstice because of lower solar irradiance received by the receiver caused by the larger cosine loss of heliostat field in the winter. Both novel receivers achieve superior performance in different seasons than the prototype receiver, demonstrating their great feasibility and practicality throughout the year. The novel receiver I and II have the largest efficiency improvement percentages of 6.13 and 6.78 % in the winter, while the lowest efficiency improvement percentages of 5.05 and 4.82 % in the summer, indicating that the novel receivers exert more effective roles in enhancing thermal performance in the winter. In addition, it is worth noting that the novel receiver I has better thermal performance than the novel

receiver II in the summer but worse thermal performance in the winter. The reason for this phenomenon is that, though the solar irradiance received in regions with the secondary coating in the summer is higher than that in the winter, it only accounts for 2.54 % of the whole solar irradiance received by the receiver, less than the proportion of 2.81 % in the winter (Fig. 13). The higher proportion of solar irradiance in regions with secondary coating, the more important is solar irradiance absorption. Thus, the high solar absorptance of black chrome-based coating exerts a more effective role in enhancing the receiver efficiency in the winter.

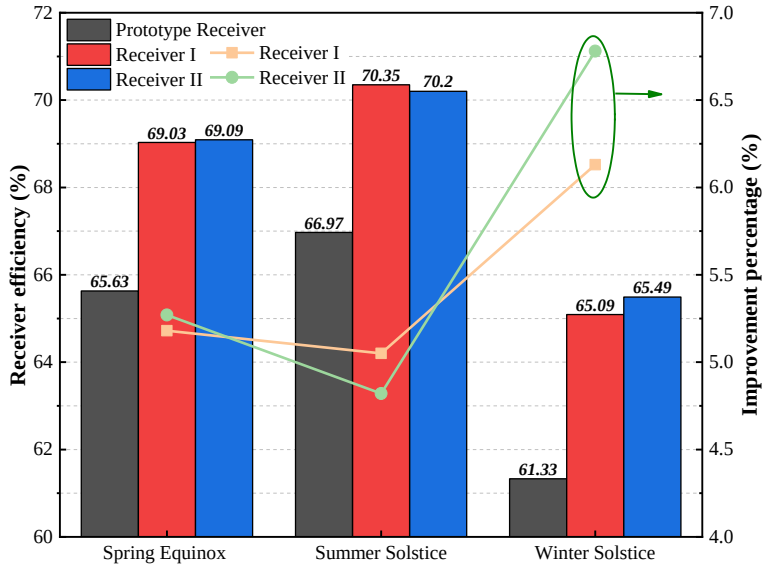

Fig. 12 Receiver efficiencies of three kinds of receivers at the noon of the spring equinox, summer solstice, and winter solstice

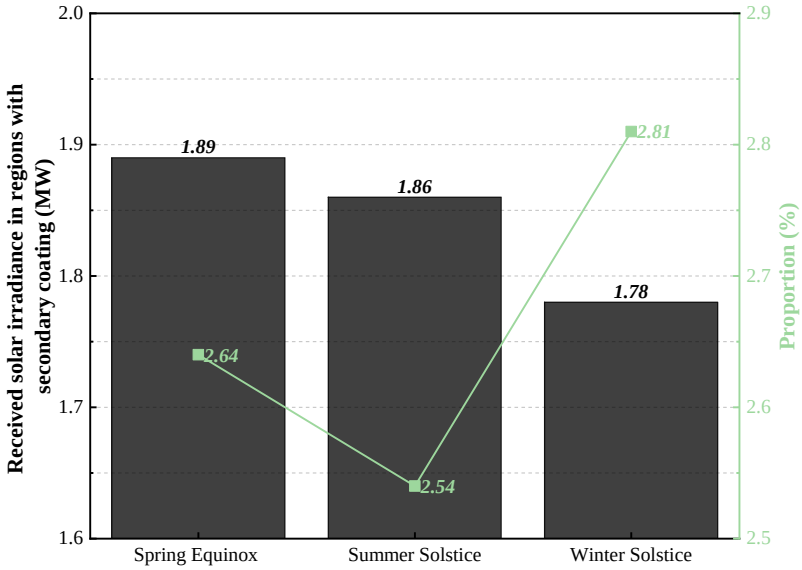

Fig. 13 Received solar irradiance in regions with the secondary coating

5. Perspective and future work

The above preliminary analyses on the novel receivers validate the good feasibility and practicality of regional SAC improvement strategy in the next-generation SPT system. This new way of employing two kinds of coatings simultaneously in the tower receiver tackles the knotty technical problem of massive radiation heat loss with extremely limited solar absorption loss. Besides, this regional SAC improvement method is expected to be simple to implement and cost-efficient. Therefore, this new tower receiver technology has a highly promising perspective for the applications in the next-generation SPT system. It is worth mentioning that the Ag-based coating is not the best material for the next-generation SPT in consideration of durability, long-term stability, and optical properties, but this extreme case using Ag-based coating is a worthy attempt for the further improvement of SAC in the SPT.

Through the above studies, it can be concluded that the secondary coating's optical properties (absorptance and emittance) exert significant roles. The optimum optical properties of the coating and the general rules will be further investigated to observe the largest potential of this improvement method in the next work. The parametric analysis, such as mass flow rate and type of flow path, will be discussed as well. Besides, the indoor experiments based on the energy balance method will be carried out to further verify the negative thermal-flux phenomenon. The detailed techno-economic analysis of the novel receivers in the real power plants will also be studied.

6. Conclusions

In this work, based on the annual average solar flux distribution on the tower receiver, negative thermal-flux phenomenon and negative thermal-flux regions (NTRs) were conceptually proposed for the next-generation SPT system. Two kinds of novel tower receivers by changing the conventional black Pyromark paint in NTRs into Ag-based coating and black chrome-based coating (novel receiver I and novel receiver II, respectively) were put forward to reduce the radiation heat loss and enhance the thermal performance. In this study, Dunhuang 10 MW CSP system was selected as the study case, and a detailed heat transfer model of the tower receiver was established. The comparisons between the

simulated results by the model and experimental data show that the established model is able to predict the thermal performance of the tower receiver with high accuracy. The RSMD of the receiver efficiency is only 0.72. In this framework, the annual average heat transfer metrics of prototype receiver, novel receivers I and II are calculated and compared. In addition, the thermal performance of novel receivers is also investigated under different *DNIs*, different solar hours throughout the day, and different seasons. The results are summarized as follows:

1) The mismatch between the solar flux distribution and radiation heat loss distribution leads to negative thermal-flux phenomena (negative net heat gains) at edge regions of the tower receiver close to the southern side. These negative thermal-flux regions account for almost a quarter of the entire receiver, which inspires us to propose a novel regional solar absorbing coating (SAC) improvement strategy.
2) The novel receiver I with Ag-based coating changes in NTRs and receiver II with black chrome-based coating changes in NTRs obtain great successes in improving the negative thermal-flux phenomenon and enhancing the receiver efficiency. The annual average radiation heat losses in regions with Ag-based coating and black chrome-based coating are effectively reduced by 93.00 and 53.14 % compared with conventional black Pyromark paint. The annual average heat gains and receiver efficiencies of novel receivers I and II have breakthrough enhancements by 6.54 and 6.03 % compared with the prototype receiver.
3) Both novel receivers achieve superior thermal performance than the prototype receiver at the *DNI* from 500 to 900 W/m^2, and the novel receiver I possesses the best performance at low *DNIs* below 750 W/m^2 while the novel receiver II surpasses the novel receiver I as the best-performance one with the *DNI* exceeding 750 W/m^2. At the *DNI* of 500 W/m^2, the improvement percentages in efficiency of the novel receivers I and II reach 11.11 and 8.9 %, respectively.
4) Both novel receivers I and II maintain superior thermal performance throughout the day. Particularly in the morning and evening, two novel receivers obtain more excellent performance. The receiver efficiencies of the novel receivers I and II are enhanced by 8.67 and 8.03 %, 3.42 and 3.74 % at 8 and 12 h, respectively.

5) Both novel receivers achieve superior performance indifferent seasons than the prototype receiver. They have the largest efficiency improvement percentages of 6.13 and 6.78 % in the winter, while the lowest efficiency improvement percentages of 5.05 and 4.82 % in the summer, indicating that the novel receivers exert more effective roles in enhancing thermal performance in the winter.

Acknowledgment

This study was sponsored by the RGC Postdoctoral Fellowship Scheme 2020/2021 (3-RA59) of the University Grants Committee and the Postdoctoral Hub program (PiH/160/19) of the Innovation and Technology Fund, the Hong Kong SAR Government.

Reference

[1] He Y L, Qiu Y, Wang K, et al. Perspective of concentrating solar power. Energy, 2020, 198: 117373.
[2] Pelay U, Luo L, Fan Y, et al. Thermal energy storage systems for concentrated solar power plants. Renewable and Sustainable Energy Reviews, 2017, 79: 82-100.
[3] D. Hales. Renewables 2020 global status report. Rep. Paris (2020), 120-130. REN2.
[4] Pitz-Paal R. Concentrating solar power: still small but learning fast. Nature Energy, 2017, 2(7): 1-2.
[5] Yu Q, Fu P, Yang Y, et al. Modeling and parametric study of molten salt receiver of concentrating solar power tower plant. Energy, 2020, 200: 117505.
[6] Wang Q, Yao Y, Hu M, et al. An air curtain surrounding the solar tower receiver for effective reduction of convective heat loss. Sustainable Cities and Society, 2021: 103007.
[7] Fuqiang W, Ziming C, Jianyu T, et al. Progress in concentrated solar power technology with parabolic trough collector system: A comprehensive review. Renewable and Sustainable Energy Reviews, 2017, 79: 1314-1328.
[8] Wang Q, Yang H, Zhong S, et al. Comprehensive experimental testing and analysis on parabolic trough solar receiver integrated with radiation shield. Applied Energy, 2020, 268: 115004.
[9] Qiu Y, Xu Y, Li Q, et al. Efficiency enhancement of a solar trough collector by combining solar and hot mirrors. Applied Energy, 2021, 299: 117290.
[10] Pavlovic S, Loni R, Bellos E, et al. Comparative study of spiral and conical cavity receivers for a solar dish collector. Energy Conversion and Management, 2018, 178: 111-122.
[11] Cheng Z D, Zhao X R, He Y L, et al. A novel optical optimization model for linear Fresnel reflector concentrators. Renewable energy, 2018, 129: 486-499.
[12] Binotti M, Astolfi M, Campanari S, et al. Preliminary assessment of sCO2 power cycles for application to CSP Solar Tower plants. Energy Procedia, 2017, 105: 1116-1122.
[13] Hussain M I, Ménézo C, Kim J T. Advances in solar thermal harvesting technology based on surface solar absorption collectors: A review. Solar Energy Materials and Solar Cells, 2018, 187: 123-139.
[14] Relloso S, Gutiérrez Y. SENER molten salt tower technology. Ouarzazate NOOR III case[C]//AIP Conference Proceedings. AIP Publishing LLC, 2017, 1850(1): 030041.

[15] Wang Q, Pei G, Yang H. Techno-economic assessment of performance-enhanced parabolic trough receiver in concentrated solar power plants. Renewable Energy, 2021, 167: 629-643.
[16] Vignarooban K, Xu X, Arvay A, et al. Heat transfer fluids for concentrating solar power systems–a review. Applied Energy, 2015, 146: 383-396.
[17] Mwesigye A, Yılmaz İ H. Thermal and thermodynamic benchmarking of liquid heat transfer fluids in a high concentration ratio parabolic trough solar collector system. Journal of Molecular Liquids, 2020, 319: 114151.
[18] Forsberg C W, Peterson P F, Zhao H. High-temperature liquid-fluoride-salt closed-Brayton-cycle solar power towers. 2007.
[19] Wang K, Li M J, Zhang Z D, et al. Evaluation of alternative eutectic salt as heat transfer fluid for solar power tower coupling a supercritical CO2 Brayton cycle from the viewpoint of system-level analysis. Journal of Cleaner Production, 2021, 279: 123472.
[20] Wang W Q, Qiu Y, Li M J, et al. Coupled optical and thermal performance of a fin-like molten salt receiver for the next-generation solar power tower. Applied Energy, 2020, 272: 115079.
[21] Boerema N, Morrison G, Taylor R, et al. High temperature solar thermal central-receiver billboard design. Solar Energy, 2013, 97: 356-368.
[22] Wang Q, Yang H, Hu M, et al. Preliminary performance study of a high-temperature parabolic trough solar evacuated receiver with an inner transparent radiation shield. Solar Energy, 2018, 173: 640-650.
[23] Yağli H. Examining the receiver heat loss, parametric optimization and exergy analysis of a solar power tower (SPT) system. Energy Sources, Part A: Recovery, Utilization, and Environmental Effects, 2020, 42(17): 2155-2180.
[24] Christian J M, Ortega J D, Ho C K. Novel tubular receiver panel configurations for increased efficiency of high-temperature solar receivers//Energy Sustainability. American Society of Mechanical Engineers, 2015, 56840: V001T05A014.
[25] Zhang L, Fang J, Wei J, et al. Numerical investigation on the thermal performance of molten salt cavity receivers with different structures. Applied energy, 2017, 204: 966-978.
[26] Ambrosini A. High-temperature solar selective coating development for power tower receivers. Sandia National Lab.(SNL-NM), Albuquerque, NM (United States). Concentrating Solar Technologies, 2016.
[27] Gray M H, Tirawat R, Kessinger K A, et al. High temperature performance of high-efficiency, multi-layer solar selective coatings for tower applications. Energy Procedia, 2015, 69: 398-404.
[28] Wang H, Haechler I, Kaur S, et al. Spectrally selective solar absorber stable up to 900° C for 120 h under ambient conditions. Solar Energy, 2018, 174: 305-311.
[29] López-Herraiz M, Fernández A B, Martinez N, et al. Effect of the optical properties of the coating of a concentrated solar power central receiver on its thermal efficiency. Solar Energy Materials and Solar Cells, 2017, 159: 66-72.
[30] Li R, Zhang H, Wang H, et al. Integrated hybrid life cycle assessment and contribution analysis for CO2 emission and energy consumption of a concentrated solar power plant in China. Energy, 2019, 174: 310-322.288
[31] http://www.cspfocus.cn/en/market/detail_972.htm
[32] Yang H, Li J, Wang Q, et al. Performance investigation of solar tower system using cascade supercritical carbon dioxide Brayton-steam Rankine cycle. Energy Conversion and Management, 2020, 225: 113430.

[33] Ho C K, Mahoney A R, Ambrosini A, et al. Characterization of Pyromark 2500 paint for high-temperature solar receivers. Journal of Solar Energy Engineering, 2014, 136(1).
[34] Rodriguez-Sanchez M R, Sanchez-Gonzalez A, Marugan-Cruz C, et al. Flow patterns of external solar receivers. Solar Energy, 2015, 122: 940-953.
[35] Polimeni S, Binotti M, Moretti L, et al. Comparison of sodium and KCl-MgCl2 as heat transfer fluids in CSP solar tower with sCO2 power cycles. Solar Energy, 2018, 162: 510-524.
[36] Xu X, Wang X, Li P, et al. Experimental test of properties of KCl–MgCl2 eutectic molten salt for heat transfer and thermal storage fluid in concentrated solar power systems. Journal of Solar Energy Engineering, 2018, 140(5).
[37] FluxSPT software. ISE Research Group. http://ise.uc3m.es/research/solar-energy/heliostat-field/.
[38] Sánchez-González A, Santana D. Solar flux distribution on central receivers: A projection method from analytic function. Renewable Energy, 2015, 74: 576-587.
[39] Sánchez-González A, Rodríguez-Sánchez M R, Santana D. Aiming factor to flatten the flux distribution on cylindrical receivers. Energy, 2018, 153: 113-125.
[40] Pacheco J E, Bradshaw R W, Dawson D B, et al. Final test and evaluation results from the solar two project. SAND2002-0120, 2002: 1-294.
[41] He Y L, Wang K, Qiu Y, et al. Review of the solar flux distribution in concentrated solar power: non-uniform features, challenges, and solutions. Applied Thermal Engineering, 2019, 149: 448-474.
[42] Bergman T L, Incropera F P, DeWitt D P, et al. Fundamentals of heat and mass transfer. John Wiley & Sons, 2011.
[43] Siebers D L, Kraabel J S. Estimating convective energy losses from solar central receivers. Sandia National Lab.(SNL-CA), Livermore, CA (United States), 1984.
[44] Wang K, He Y L, Xue X D, et al. Multi-objective optimization of the aiming strategy for the solar power tower with a cavity receiver by using the non-dominated sorting genetic algorithm. Applied Energy, 2017, 205: 399-416.
[45] Wang Q, Shen B, Huang J, et al. A spectral self-regulating parabolic trough solar receiver integrated with vanadium dioxide-based thermochromic coating. Applied Energy, 2021, 285: 116453.
[46] Wang Q, Yang H, Hu M, et al. Optimization strategies and verifications of negative thermal-flux region occurring in parabolic trough solar receiver. Journal of Cleaner Production, 2021, 278: 123407.
[47] https://energyplus.net/weather
[48] Sun C, Sun H F, Wang Z Y, et al. Experiment and analysis on radiation properties of SiO2/Ag optical solar reflector coating. Aerospace Science and Technology, 2018, 82: 372-377.